MOBILITY PERFORMENCE OF CILIARY LOCOMOTION FOR AN ASTEROID EXPLORATION ROBOT UNDER VARIOUS EXPERIMENTAL CONDITIONS

*Kenji Nagaoka[1], Kazuki Watanabe[2], Toshiyasu Kaneko[3], Kazuya Yoshida[4]

[1] *Tohoku University, Aoba 6-6-01, Aramaki, Aoba-ku, Sendai, Japan, E-mail: nagaoka@astro.mech.tohoku.ac.jp*
[2] *Tohoku University, Aoba 6-6-01, Aramaki, Aoba-ku, Sendai, Japan, E-mail: watanabe@astro.mech.tohoku.ac.jp*
[3] *Tohoku University, Aoba 6-6-01, Aramaki, Aoba-ku, Sendai, Japan, E-mail: kaneko@astro.mech.tohoku.ac.jp*
[4] *Tohoku University, Aoba 6-6-01, Aramaki, Aoba-ku, Sendai, Japan, E-mail: yoshida@astro.mech.tohoku.ac.jp*

ABSTRACT

This paper investigates the mobility of ciliary locomotion based on experimental and theoretical analysis. A ciliary locomotion mechanism actuated by an eccentric motor is one possible solution for enhancing mobility on a microgravity asteroid with environmental uncertainties. The proposed mechanism is also feasible for space applications because it is efficient, simple, and reliable. So far, we have evaluated the feasibility of ciliary locomotion based on mobility experiments using a microgravity emulation system and model-based numerical simulations under limited conditions. Thus, this paper discusses the mobility performance of ciliary locomotion under various environmental conditions like gravity and friction via experiments and simulations. As a result, we introduce the interaction mechanics of ciliary locomotion within a more systematic framework.

1 INTRODUCTION

The robotic exploration of small bodies such as asteroids has received attention in recent years. The Hayabusa project is the world's first sample return mission demonstrated by the Japan Aerospace eXploration Agency (JAXA). The Hayabusa spacecraft carried a small exploration robot named MINERVA [1]. MINERVA has an inner torquer and can hop using the torquer's reaction torque in microgravity. Although MINERVA's landing onto the surface was unsuccessful, the development of MINERVA has enhanced the research on robotic locomotion under microgravity. Following this mission, JAXA is now operating the Hayabusa 2 mission [2]. The Hayabusa 2 spacecraft targets the near-Earth C-type asteroid 1999 JU3 (Ryugu) and aims to arrive at Ryugu in mid-2018. Observation and analysis from Earth shows that Ryugu has an effective diameter of 870 ± 30 m, a rotation period of 7.6 h, and its shape is also nearly spherical [3]. To advance robotic exploration on the asteroid surface, several MINERVA-II rovers are installed in the Hayabusa 2 spacecraft [4, 5]. Figure 1 shows the MINERVA-II2 system,

Figure 1 : Flight model of the MINERVA-II2 system © MINERVA-II Consortium.

which is one of the MINERVA-II systems developed by the MINERVA-II University Consortium [5].

Hopping mobility is one possible solution to locomotion on a microgravity asteroid. So far, various other hopping mechanisms have been proposed for an asteroid exploration robot in addition to the MINERVA's hopping mechanism [6–14]. We proposed a ciliary locomotion mechanism actuated by a vibration motor [9, 10], whereas most of the other hopping mechanisms hop by a relatively-larger impulsive force from the ground surface. The ciliary locomotion robot can crawl and perform micro-hops, and achieves more accurate locomotion in microgravity. This mechanism was equipped with the MINERVA-II2 Rover 2 and will be demonstrated on the mission as one of the engineering challenges [5]. Although the fundamental mobility performance and feasibility of ciliary locomotion robot has been discussed based on theoretical and experimental analyses [9, 10], the effect of the environmental parameters, such as gravity, friction, or surface irregularity, on performance remains to be elucidated.

We address ciliary locomotion mechanics with environmental variations in microgravity. In particular, the environment on the surface of an asteroid is highly uncertain. To maximize and appropriately control the mobility of ciliary locomotion, a more systematic understanding based on experimental and theoretical approaches is necessary. In this paper, the interaction mechanics of ciliary locomotion is shown through an analysis of the mobility performance, which is examined by experiment and simulation.

This paper is organized as follows. Section 2 presents the locomotion principles of the ciliary locomotion robot based on microscale observation by a camera. The fundamental framework of the locomotion performance is also described. Section 3 introduces the experimental analysis of the ciliary locomotion robot under various environmental conditions: gravity, friction, and surface slope. The experimental results exhibit the mobility performance more systematically. Section 4 presents a theoretical model of the locomotion system, and then the results of the experiments and simulation are compared. The comparison yields a key relationship from the viewpoint of interaction mechanics. Section 5 summarizes the results and contributions of this paper.

2 CILIARY LOCOMOTION PRINCIPLES

Ciliary locomotion is an innovative mobility system that utilizes the elastic force of cilia attached to the robot surface at an angle. Utilizing vibratory actuation and the deflection/buckling of the cilia, the robot is propelled smoothly on the surface. The inclined cilia exert thrust force repeatedly by deflection and buckling based on contact with the locomotion surface. Here, the period of vibrating motion of the robot significantly affects mobility performance. In this study, we utilize an eccentric motor to exert vibratory force on the robot.

In a microgravity environment, dynamic forces become quite small. Hence, ciliary locomotion in microgravity can perform two different locomotion modes: crawling and hopping [9, 10]. Figure 2 illustrates these modes. In particular, the hopping height is quite small in a nominal case, and thus we call it micro-hopping. Ciliary locomotion is based on a complicated dynamic interaction between the cilia and locomotion surface. To better illustrate the locomotion principle, this paper first presents observed results of microscale cilia behavior during locomotion.

2.1 High-Speed Camera Observation

2.1.1 Experimental Setup

We observed the precise microscale motion of a cilium through planar microgravity experiments. Figure 3 shows an overview of the experimental environment. For the experimental analysis, we developed an air-floating test bed of the ciliary locomotion robot that can emulate planar motion in microgravity, as shown in Figure 4. The test bed weighs 3.85 kg, and its size is 200 × 200 mm in the *X*-*Y* plane. Figures 5(a) and (b) also show the eccentric motor unit and cilia unit mounted on the test bed. The eccentric weight weighs 12 g and the eccentric distance is 3.9 mm. The cilia in the cilia unit are made of nylon, and their inclination angle is 80°. The cilia bundles are attached in five rows and eight columns. Throughout these experiments, the gravity level was set to 1×10^{-3} G. The test bed can be controlled by an on-board micro-controller, and we input the motor frequency as a command via wireless communication. Figure 6 shows the electrical system configuration of the test bed. The planar motion of the test bed was also obtained by an external motion capture camera system.

We observed the microscale behavior of the cilia using a VW-9000 high-speed camera produced by KEYENCE Corporation, Japan. A VW-Z2 lens was used (KEYENCE Corporation), and close-up views within a 5 mm radius were obtained during the locomotion experiments. The obtained video resolution is 640 × 480 pixels, and the frame rate was set to 1 kHz.

2.1.2 Results and Discussion

An example image taken by the camera is shown in Figure 7. From these observations, the cilium motion can be summarized as the mode of which the deflection and buckling of the cilium is (i) increasing or (ii) decreasing. Furthermore, in principle, each mode can also be divided into the following four motion states.

- Negative slip:
  The cilium slips in a negative direction with respect to the locomotion. The ciliary thrust works in a positive direction with respect to the locomotion.

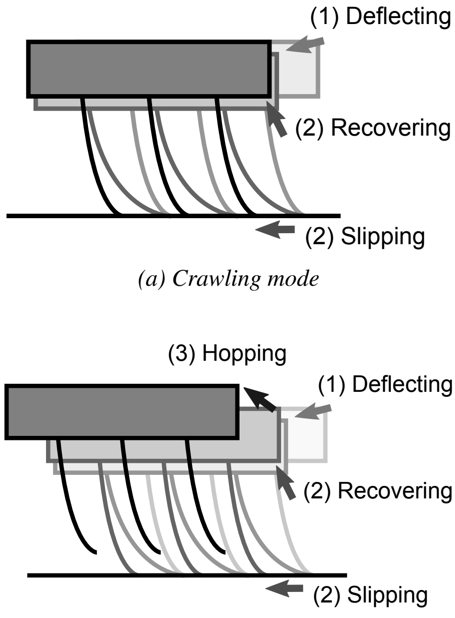

(a) Crawling mode

(b) Hopping mode

Figure 2 : Schematic illustration of ciliary locomotion.

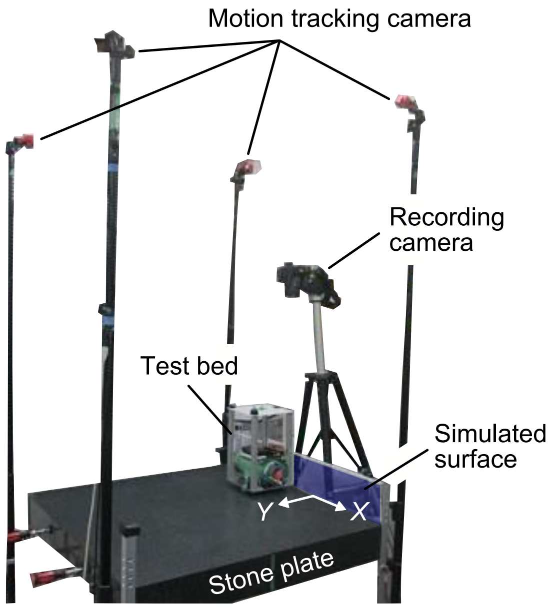

Figure 3 : Experimental overview of the microgravity emulation and measurement system.

- Sticking:
  The cilium tip sticks to the surface. Basically, the ciliary thrust works in a positive direction with respect to the locomotion.

- Positive slip:
  The cilium slips in a positive direction with respect to the locomotion. The ciliary thrust works in a negative direction with respect to the locomotion. Large locomotion velocities induce this state.

- Hopping:
  The cilium does not contact the surface. No reaction force is assumed.

Based on the observation results, we confirmed that ciliary locomotion is achieved by alternating modes (i) and (ii). In particular, we observed that the tip of a cilium holds onto the surface when it is deformed in most situations. In contrast, the tip mostly slips in a direction that is opposite to that of the locomotion when recovering from deflection and buckling. When the cilia maintain contact with the surface, stable ciliary locomotion can be performed. The observed motion was basically the crawling mode because of the irregular properties of the cilia at microscale. This result is also the same behavior as reported for ciliary locomotion on a surface under 1 G [15].

3 EXPERIMENTAL MOBILITY PERFORMANCE

This section presents the results of the experimental mobility performance obtained using the air-floating test bed, which emulates motion in a microgravity environment. In particular, the effects of gravity level and roughness of surface on the mobility of ciliary locomotion were experimentally investigated.

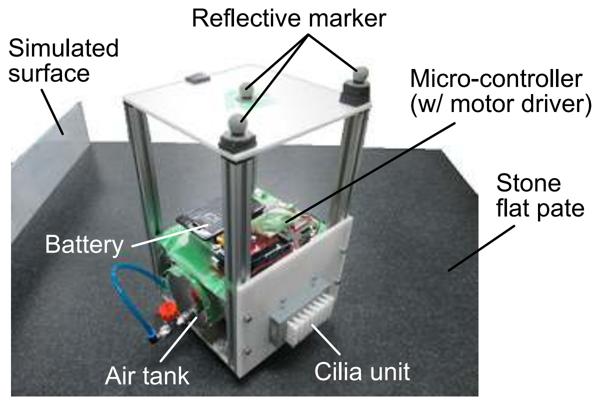

Figure 4 : Ciliary locomotion robot test bed for microgravity experiments.

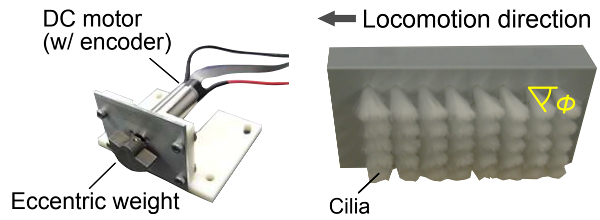

(a) Eccentric motor *(b) Cilia unit*

Figure 5 : Overview of the test bed actuation system.

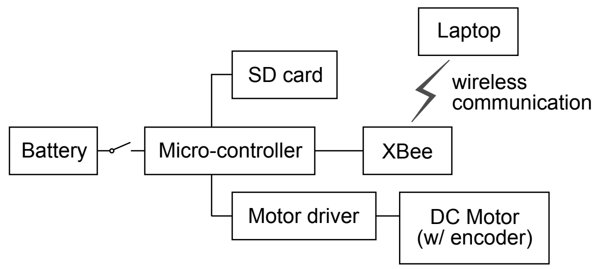

Figure 6 : Electrical system configuration of the test bed.

3.1 Flat Surface Experiments

3.1.1 Experimental Conditions

For the locomotion experiments on an acrylic flat surface, we investigated the effects of different levels of the emulated gravity and motor frequencies to analyze the locomotion parameters. The experimental conditions were as follows:

- Gravity: 1×10^{-2} G, 5×10^{-3} G, and 1×10^{-3} G

- Motor Frequency: 5 Hz ~ 80 Hz in intervals of 5 Hz

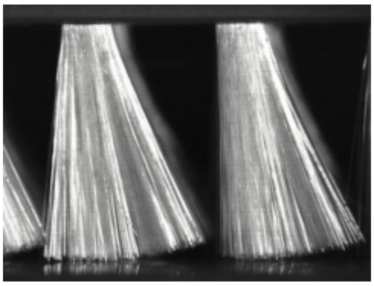

Figure 7 : Example high-speed camera image of cilia during locomotion.

For each condition, we conducted five trials and averaged the locomotion velocity with error bars. The level of the emulated gravity was adjusted by changing the inclination angle of the stone plate. We then quantitatively evaluated the gravity by analyzing the free motion of the test bed. The gravity in the x-axis direction was set within a $\pm 5\%$ error, and in the y-axis direction was adjusted to be less than $\pm 1\%$ of the value in the x-axis direction.

3.1.2 Results and Discussion

Figure 8 shows example images of the experimental motion of the test bed. In almost all of the cases, the test bed moved smoothly without body rotation. Figure 9 depicts the relationship between the motor frequency and linear locomotion velocity of the test bed. This graph summarizes the results for each gravity condition, and shows that gravity affects the locomotion velocity. That is, a larger gravity results in a smaller locomotion velocity in these cases. Friction force is a major factor here. A larger gravitational force leads to more deflection and buckling of the cilium because of the greater robot weight. Although this exerts a larger elastic force on the robot, at the same time, the friction force works as a larger negative factor when the cilia are recovering from the deflection and buckling.

In addition, under $g = 1 \times 10^{-3}$ [G], a clear peak in velocity is seen at around $f = 35$ [Hz]. We call this the state transition point. Whereas the velocity is proportional to the motor frequency from 0 Hz to 35 Hz, it increases as a second order curve of the frequency at more than 40 Hz. These observed results come from the resonant characteristic of elastic deflection and buckling of the cilia at around $f = 35$ [Hz]. Therefore, at frequencies higher than the resonant frequency, a decline in the locomotion velocity was generated because the amplitude of the test bed vertical motion decreased. In contrast, at more than $f = 80$ [Hz], the locomotion velocity rapidly increases. This comes from a resonant characteristic of the mechanical stiffness of the test bed. This mechanical resonant frequency was also observed by a vibration sensor attached to the test bed. The resonant frequency generates a larger vertical motion amplitude, affects the cilia's deflection and buckling, and as a result, the locomotion velocity increases. This tendency is notable at $g = 1 \times 10^{-3}$ [G], but it is a characteristic that is not of particular note in the other gravity cases.

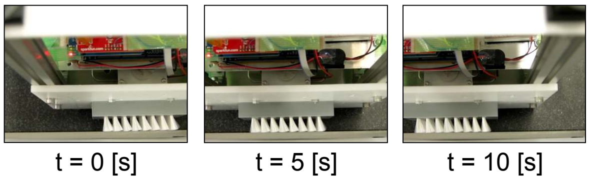

Figure 8 : Example image of the experimental motion of the test bed: $g = 1 \times 10^{-3}$ [G] and $f = 30$ [Hz].

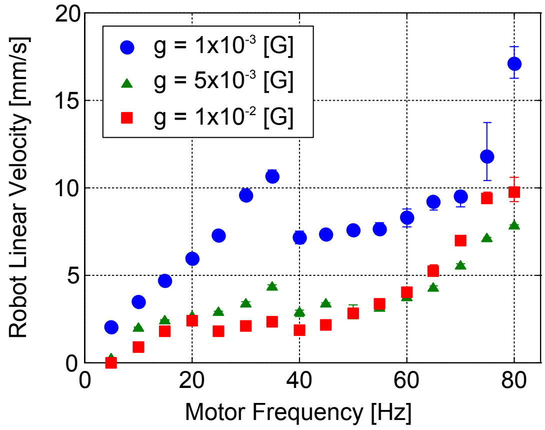

Figure 9 : Experimental results for steady locomotion velocity on an acrylic flat surface for various levels of emulated gravity.

3.2 Frictional Sloped Surface Experiments

3.2.1 Experimental Conditions

The mobility performance on a discontinuous sloped surface was experimentally investigated. In the experiments, the gravity was set to $g = 1 \times 10^{-3}$ [G]. The motor frequency was selected from 10 Hz to 80 Hz in interval of 10 Hz. Figure 10 shows the flat and sloped surface used. Moreover, a sheet of sandpaper was attached on the locomotion surface to investigate the effects of friction on mobility. As the key experimental conditions, the slope inclination angle and grit of the sandpaper were set as follows:

- Sandpaper: #120 (rough), #320, and #1000 (smooth)
- Slope angle (α): 2°, 4°, 6°, 8°, and 10°

3.2.2 Results and Discussion

Figure 11 shows the experimental results of locomotion velocity on the sandpaper and acyclic board (for reference), where the velocity was obtained from trials on a flat surface area (not a slope). The results confirm that lower friction works better for the locomotion velocity. Although higher friction generates larger propulsive thrust

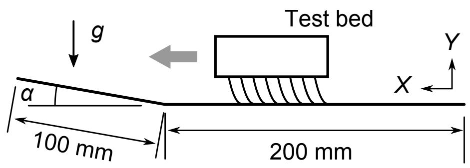

Figure 10 : Schematic of ciliary locomotion experiments on a discontinuous surface with a slope.

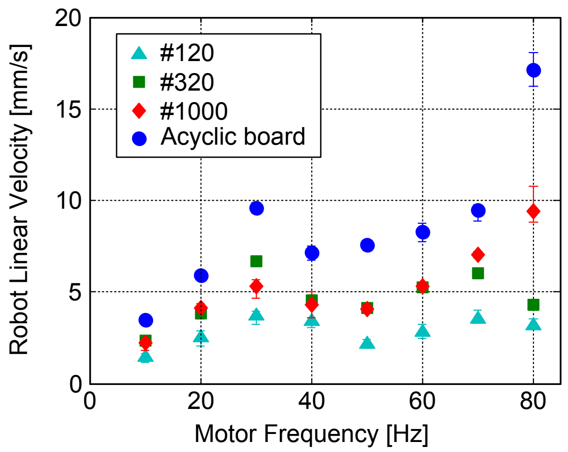

Figure 11 : Experimental results for steady locomotion velocity on flat sandpaper: $g = 1 \times 10^{-3}$ [G].

from a general standpoint, it simultaneously creates larger resistance. Therefore, as a design factor, the cilia must be designed to maximize the mobility on an uncertain asteroid surface considering its frictional properties.

Table 1 shows the experimental results of slope traveling, where a check-mark (✓) indicates that the test bed was able to move on the slope. The locomotion on a surface covered with #320 sandpaper, which is a surface with medium friction, showed better slope traveling performance. This comes from the trade-off between thrust force and frictional resistance. The results also show that the slope traveling performance depends on the locomotion velocity. In contrast, the locomotion on the acyclic board (low friction) achieved higher velocity than on the sandpaper. Although a trade-off exits, the results confirm that lower friction leads to better locomotion performance.

4 THEORETICAL ANALYSIS

This section introduces the dynamics model of ciliary locomotion, and then presents its numerical analysis. The theoretical model is validated by a comparison with the experimental results, and we provide key remarks regarding the mechanics of ciliary locomotion.

4.1 Dynamics Model

4.1.1 Equations of Motion

In this section, we introduce a planar dynamics model of the ciliary locomotion robot. This paper assumes a two-dimensional dynamics model. Figure 12 illustrates the schematic of the ciliary locomotion robot dynamics model. We extended the fundamental dynamics model developed in [16]. In this study, the locomotion surface is assumed to be uniform and flat. We first define the inertia coordinate $\Sigma_O\{X, Y\}$, in which X is the horizontal axis parallel to the terrain surface and Y is the vertical axis normal to the X-axis. The origin of the Y-axis is fixed at the locomotion surface. In addition, $\Sigma_R\{x, y\}$ denotes the robot-fixed coordinates as shown in Figure 12(a). The equations of motion of the robot with n cilia bundles are derived as follows:

$$M\ddot{X}_G = \boldsymbol{F_m} \cdot \boldsymbol{X} + \sum_{i=1}^{n} F_{fi} \tag{1}$$

$$M\ddot{Y}_G = \boldsymbol{F_m} \cdot \boldsymbol{Y} - Mg + \sum_{i=1}^{n} \boldsymbol{F_i} \cdot \boldsymbol{Y} \tag{2}$$

$$J\ddot{\theta} = \boldsymbol{g_m} \otimes \boldsymbol{F_m} - \tau_m + \sum_{i=1}^{n} (\boldsymbol{r_i} \otimes \boldsymbol{F_i} - T_i) \tag{3}$$

where M is the robot mass, X_G and Y_G are the position of the center of gravity (COG) of the robot in Σ_O, $\boldsymbol{X}$ and $\boldsymbol{Y}$ are the unit vectors of the X- and Y-axis, respectively, J is the moment of inertia of the robot around its COG, θ is the rotation angle of the robot around its COG (where counter-clockwise is positive), $\boldsymbol{F_m}$ is the centrifugal force exerted by the eccentric motor, F_{fi} is the friction force between the i-th cilia and the terrain, g is gravitational acceleration, $\boldsymbol{F_i}$ is the force exerted by the i-th cilia on the robot body, $\boldsymbol{r_i}$ is the vector from the COG to the base of the i-th cilia in Σ_R, $\boldsymbol{g_m}$ is the vector from the COG to the rotational axis of the motor, and T_i is the viscous-elastic torque exerted on the based of the i-th cilia. Here, we can assume $\tau \approx 0$ because of the very small moment of inertia of the eccentric weight. Furthermore, g_{mx} and g_{my} are also approximated as 0 in the actual test bed design.

4.1.2 Contact Detection and Mechanics

Given $(p_{i_{X0}}, p_{i_{Y0}})$ is the ideal tip position of the i-th cilia without deformation in Σ_O (where $i = 1, \cdots, n$), $p_{i_{X0}}$ and $p_{i_{Y0}}$ can be geometrically written as follows:

$$\begin{cases} p_{i_{X0}} = X_G + r_{ix}\cos\theta - r_{iy}\sin\theta - h_{i0}\cos(\theta + \phi_{i0}) \\ p_{i_{Y0}} = Y_G + r_{ix}\sin\theta + r_{iy}\cos\theta - h_{i0}\sin(\theta + \phi_{i0}) \end{cases} \tag{4}$$

where r_{ix} and r_{iy} are the x and y components of $\boldsymbol{r_i}$ in Σ_R, respectively. In addition, h_{i0} and ϕ_{i0} are the natural length and implant angle of the cilia, respectively.

Table 1 : Experimental ability of the test bed to climb slopes with various frictional surfaces.

Sandpaper	#1000					#320					#120				
Slope angle	2°	4°	6°	8°	10°	2°	4°	6°	8°	10°	2°	4°	6°	8°	10°
f = 10 [Hz]	✓					✓	✓	✓			✓	✓			
f = 20 [Hz]	✓					✓	✓	✓			✓	✓			
f = 30 [Hz]	✓	✓				✓	✓	✓			✓	✓			
f = 40 [Hz]	✓					✓	✓				✓				
f = 50 [Hz]	✓	✓				✓	✓				✓				
f = 60 [Hz]	✓	✓				✓	✓	✓			✓				
f = 70 [Hz]	✓	✓	✓			✓	✓	✓			✓				
f = 80 [Hz]	✓	✓	✓	✓		✓	✓	✓			✓				

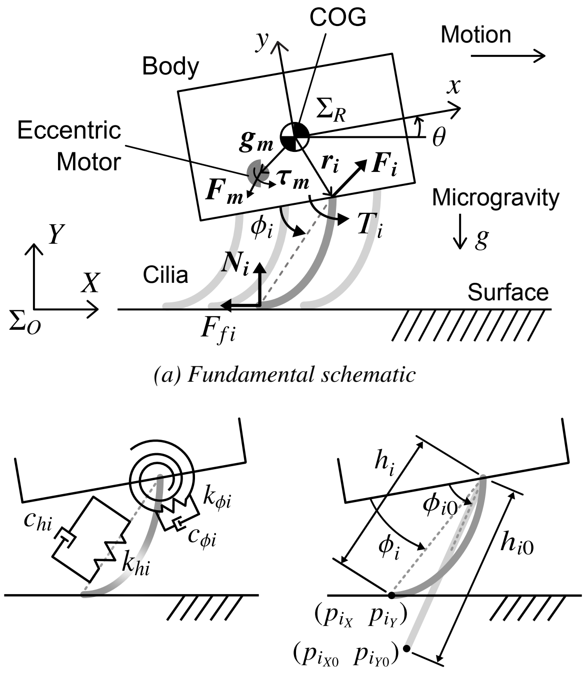

(a) Fundamental schematic

(b) Interaction mechanics *(c) Deformation of cilia*

Figure 12 : Dynamic model of ciliary locomotion robot.

Assuming the cilia deformation (deflection and buckling) is quite small, the reaction force $\boldsymbol{F_i} \equiv (F_{i_X}, F_{i_Y})$ in Σ_O generated by the cilia can be given as follows:

- $p_{i_Y} > 0$:

$$F_{i_X} = F_{i_Y} = 0 \tag{5}$$

- $p_{i_Y} \leq 0$:

$$\begin{cases} F_{i_X} = F_{h_i}\cos(\phi_i + \theta) - \dfrac{T_i \sin(\phi_i + \theta)}{h_i} \\ F_{i_Y} = F_{h_i}\sin(\phi_i + \theta) + \dfrac{T_i \cos(\phi_i + \theta)}{h_i} \end{cases} \tag{6}$$

Furthermore,

$$F_{h_i} = k_{h_i}(h_{i0} - h_i) - c_{h_i}\dot{h}_i \tag{7}$$

$$T_i = k_{\phi_i}(\phi_{i0} - \phi_i) - c_{\phi_i}\dot{\phi}_i \tag{8}$$

where F_{h_i} is the elastic deflection force, T_i is the viscoelastic torque, and h_i and ϕ_i are the equivalent cilia length and bucking angle, respectively. Furthermore, k_{h_i} and k_{ϕ_i} are the elastic stiffnesses, and c_{h_i} and c_{ϕ_i} are the damping coefficients. When restoring the cilia from a deformed state to a natural one (i.e., $\dot{h}_i \geq 0$ and $\dot{\phi}_i \geq 0$), the damping coefficients c_{h_i} and c_{ϕ_i} are assumed to be zero.

4.1.3 Contact Point Determination

The contact point must be determined to calculate the reaction force when contact is detected by Eq. (4). We here assume a small time step for the integral calculation of a discrete-time system as a quasi-static analysis. First, contact force F_{i_X} is calculated based on the assumption that the cilia are sticking to the surface. When this condition is satisfied, i.e., $|F_{i_X}| < \mu_0 F_{i_Y}$, where μ_0 is the maximum coefficient of static friction, contact point p_{i_X} maintains its contact in the last time step. If the condition is not satisfied, ϕ_i is iteratively changed so that $|F_{i_X}| < \mu_0 F_{i_Y}$, p_{i_X} decreases with respect to negative slip ($F_{i_X} > 0$) and increases with respect to positive slip ($F_{i_X} < 0$). On the basis of this analysis, we can define the cilia's deformation parameters, h_i and ϕ_i, as follows:

- Negative and positive slip:

$$\begin{cases} h_i = \dfrac{Y_G + r_{ix}\sin\theta + r_{iy}\cos\theta}{\sin(\theta + \phi_i)} \\ \phi_i = \hat{\phi}_i - \mathrm{sgn}(F_{i_X})\, s\Delta\phi \end{cases} \tag{9}$$

- Sticking:

$$\begin{cases} h_i = \Big\{\left(Y_G + r_{ix}\sin\theta + r_{iy}\cos\theta\right)^2 \\ \qquad + \left(X_G + r_{ix}\cos\theta - r_{iy}\sin\theta - \tilde{p}_{i_X}\right)^2\Big\}^{\frac{1}{2}} \\ \phi_i = \hat{\phi}_i \end{cases} \tag{10}$$

- Hopping:

$$\begin{cases} h_i = h_{i0} \\ \phi_i = \phi_{i0} \end{cases} \tag{11}$$

Here, $\tilde{p}_{i_X}$ is the tip position of p_{i_X} on the last calculation step in Σ_O is satisfied, s is the minimum value so that $F_{i_X} < \mu_0 F_{i_Y}$, $\Delta\phi$ is a small calculation step for incrementing ϕ_i, $\mathrm{sgn}\,(\cdot)$ is a signal function, and $\hat{\phi}_i$ is given as follows:

$$\hat{\phi}_i = \tan^{-1}\left(\frac{Y_G + r_{ix}\sin\theta + r_{iy}\cos\theta}{X_G + r_{ix}\cos\theta - r_{iy}\sin\theta - \tilde{p}_{i_X}}\right) - \theta \tag{12}$$

The deflection and buckling states of the cilia under slip are determined by the iterative calculation, and we can then compute the definitive reaction force $\boldsymbol{F_i}$ to be applied at the current time step.

4.1.4 Frictional Characteristics

We apply the static and kinetic friction forces depending on the motion velocity. For the four motion states defined in the previous section, F_{fi} can be given as follows:

- Negative slip:

$$F_{fi} = \mu F_{i_Y} \tag{13}$$

- Sticking:

$$F_{fi} = F_{i_X} \quad (< \mu_0 F_{i_Y}) \tag{14}$$

- Positive slip:

$$F_{fi} = -\mu F_{i_Y} \tag{15}$$

- Hopping:

$$F_{fi} = 0 \tag{16}$$

where μ is the coefficient of kinetic friction.

4.1.5 Eccentric Motor

The centrifugal force $\boldsymbol{F_m} \equiv (F_{m_X}, F_{m_Y})$ in Σ_O exerted by the eccentric motor can be represented as follows:

$$\begin{cases} F_{m_X} = m r_m \omega^2 \cos(\Omega + \theta) \\ F_{m_Y} = m r_m \omega^2 \sin(\Omega + \theta) \end{cases} \tag{17}$$

where m is the mass of the eccentric weight, r_m is the eccentric distance between the motor's rotational axis and the position of the center of mass of the eccentric weight, ω is the motor angular velocity, and Ω is the motor's rotating angle. According to its definition, we derive $\Omega = \int_0^t \omega{\cdot}dt$ (boundary conditions: $\Omega = \Omega_0$ and $\omega = \omega_0$ at $t = 0$). In the analysis, we define motor frequency f as $f = \omega/2\pi$ [Hz].

4.2 Comparative Analysis

The model-based numerical simulations were performed for comparison with the experimental results. This paper presents comparative analysis of ciliary locomotion in microgravity. In particular, this analysis focuses on the state transition point at around $f = 35$ [Hz].

4.2.1 Simulation Parameter

The fundamental simulation parameters are shown in Table 2. Most of the parameters were determined so that they simulated the specifications of the test bed. Here, h_{i0} and ϕ_{i0} were given as constant values, defined as h_0 and ϕ_0, respectively. The elastic stiffness of the cilia, k_{h_i} and k_{ϕ_i}, were experimentally determined by applied weights and static deformation. In contrast, the damping coefficients, c_{h_i} and c_{ϕ_i}, were tuned through parametric analysis. Assuming no difference between the cilia, k_{h_i}, c_{h_i}, k_{ϕ_i}, and c_{ϕ_i} can be given as constant values k_h, c_h, k_ϕ, and c_ϕ, respectively. The time step was 0.1 ms in the integral calculation.

4.2.2 Results and Discussion

Figure 13 compares the results of the experiments and model-based simulations. These plots show the data of the locomotion velocity on an acyclic flat surface in $g = 1 \times 10^{-3}$ [G]. The model can qualitatively simulate the experimental mobility performance. In particular, the results confirm that the simulation produces the same state transition point as the experiments at around around $f = 35$ [Hz]. This arises from the resonance of the motor frequency with the cilia's stiffness. Assuming the robot is a simple mass-spring model, the natural frequency of the cilia is close to 35 Hz. The simulation results before the transition point match the experiments quantitatively. In contrast, the experimental and simulated velocities after the transition point have a few differences. Although most of the physical parameters of the cilia were set to constant values, variable and nonlinear parameters need to be introduced to improve the model.

5 CONCLUSION

This paper presented the experimental mobility performance of ciliary locomotion under various values of gravity, friction, and slope. In an initial approach, the locomotion principles of ciliary locomotion were observed and analysed by microscale images of a high-speed camera. Locomotion experiments were next conducted using an air-floating test bed that can emulate free motion in planar microgravity, and the results confirmed that the locomotion velocity is improved in lower gravity. Furthermore, we found that the state transition point, around 35 Hz in the test bed, results from the resonance of the motor frequency with the cilia's stiffness. The locomotion velocity was proportional to the motor frequency before the transition point, whereas the velocity descends rapidly and increases again as a quadratic curve above this point. In addition, locomotion experiments were performed on various roughness of sandpapers and slopes. As a result, although higher friction lowers locomotion velocity on a flat surface, some friction is required for the test bed to climb slopes. This reveals an important trade-off relation in the

Table 2 : Fundamental simulation parameters.

ROBOT SYSTEM		ELASTIC CILIA	
Symbol	Value	Symbol	Value
M	3.85 kg	n	8
J	0.046 kgm^2	h_0	0.015 m
m	0.012 kg	ϕ_0	$4\pi/9$ rad $(=80°)$
r_m	0.0039 m	$\mu\ (<\mu_0)$	0.25 (< 0.28)
g_{mx}	0 m	k_h	10000 N/m
g_{my}	0 m	c_h	2 Ns/m
Ω_0	0 rad	k_ϕ	0.01 Nm/rad
ω_0	0 rad/s	c_ϕ	0.00001 Nms/rad

design process. On the basis of the observed results, we developed and extended the dynamics model of the ciliary locomotion. Slip detection and frictional characteristics were introduced into the model. In particular, the model-based simulations can produce the state transition point observed in the experiments. The comparative analysis of the experiments and model-based simulations confirmed that the developed model can simulate the mobility experimentally observed on a microgravity surface.

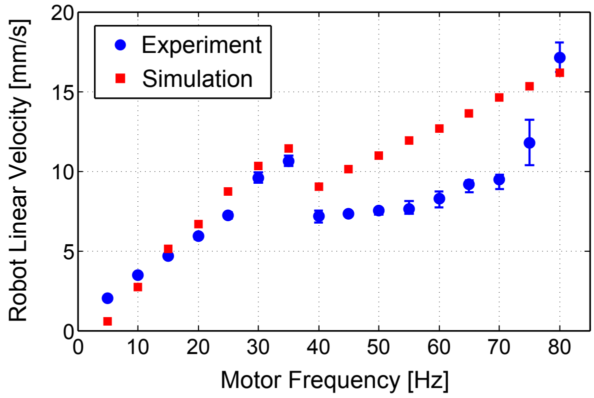

Figure 13 : Comparative results of locomotion velocity on a flat acyclic surface: $g = 1 \times 10^{-3}$ [G].

References

[1] T. Yoshimitsu, T. Kubota, I. Nakatani, T. Adachi, and H. Saito, "Micro-Hopping Robot for Asteroid Exploration", *Acta Astronautica*, vol. 52, no. 2-6, pp. 441–446, 2003.

[2] Y. Tsuda, M. Yoshikaw, M. Abe, H. Minamino, and S. Nakazawa, "System Design of the Hayabusa 2 – Asteroid Sample Return Mission to 1999 JU3", *Acta Astronautica*, vol. 91, pp. 356–362, 2013.

[3] T. G. Müller, et al., "Thermo-Physical Properties of 162173 (1999 JU3), a Potential Flyby and Rendezvous Target for Interplanetary Missions", *Astronomy and Astrophysics*, vol. 525, A145, 2011.

[4] T. Yoshimitsu, T. Kubota, A. Tomiki, and Y. Kuroda, "Development of Hopping Rovers for a New Challenging Asteroid", *Proceedings of the 12th International Symposium on Artificial Intelligence, Robotics and Automation in Space*, #5C-01, 2014.

[5] K. Nagaoka et al., "Development of MINERVA-II2, a Micro-Robot for Asteroid Surface Exploration with Innovative Mobility", *The 11th Low-Cost Planetary Missions Conference*, 2015.

[6] B. H. Wilcox and R. N. Jones, "The MUSES-CN Nanorover Mission and Related Technology", *Proceedings of the 2000 IEEE Aerospace Conference*, vol. 7, pp. 287–295, 2000.

[7] P. Fiorini and J. Burdick, "The Development of Hopping Capabilities for Small Robots", *Autonomous Robots*, vol. 14, no. 2, pp. 239–254, 2003.

[8] S. Ulamec et al., "Hopper Concepts for Small Body Landers", *Advances in Space Research*, vol. 47, no. 3, pp. 428–439, 2011.

[9] K. Nagaoka, R. Takano, T. Izumo, and K. Yoshida, "Ciliary Micro-Hopping Locomotion of an Asteroid Exploration Robot", *Proceedings of the 11th International Symposium on Artificial Intelligence, Robotics and Automation in Space*, #6A-04, 2012.

[10] K. Nagaoka and K. Yoshida, "Modeling and Analysis of Ciliary Micro-Hopping Locomotion Actuated by an Eccentric Motor in a Microgravity", *Proceedings of the 2013 IEEE/RSJ International Conference on Intelligent Robots and Systems*, pp. 763–768, 2013.

[11] M. Kurisu, "Novel Hopping Mechanism Using Permanent Magnets for Tiny Asteroid Exploration Rover", *Proceedings of the 11th International Symposium on Artificial Intelligence, Robotics and Automation in Space*, #6A-03, 2012.

[12] Y. Tsumaki, T. Akaike, R. Kazama, T. Mineta, and R. Tadakuma, "Environment-Driven Rover for Asteroid Exploration", *Proceedings of the 11th International Symposium on Artificial Intelligence, Robotics and Automation in Space*, #P-20, 2012.

[13] B. Hockman, A. Frick, I. A. D. Nesnas, and M. Pavone, "Design, Control, and Experimentation of Internally-Actuated Rovers for the Exploration of Low-Gravity Planetary Bodies", *Proceedings of the 10th Conference on Field and Service Robotics*, #42, 2015.

[14] J. T. Grundmann et al., "Mobile Asteroid Surface Scout (MASCOT) – Design, Development and Delivery of a Small Asteroid Lander Aboard Hayabusa2". *Proceedings of the 4th IAA Planetary Defense Conference*, #IAA-PDC-15-P-64, 2015.

[15] M. Konyo, K. Isaki, K. Hatazaki, S. Tadokoro, and F. Takemura, "Ciliary Vibration Drive Mechanism for Active Scope Cameras", *Journal of Robotics and Mechatronics*, vol. 20, no. 3 pp. 490–499, 2008.

[16] K. Ioi, "A Mobile Micro-Robot Using Centrifugal Forces", *Proceedings of the 1999 IEEE/ASME International Conference on Advanced Intelligent Mechatronics*, pp. 736–741, 1999.